PIER C

(Received 14 March 2026, Accepted 21 April 2026, Scheduled 1 May 2026)

A Hybrid Strategy for EMI Suppression in IPMSM Drives: Integrating Active Common-Filter with Harmonic Suppression Reaching Law

Han Lin[1], Weiran Zheng[1], Zhonggen Wang[1], and Wenyan Nie[2,*]

[1] *School of Electrical and Information Engineering, Anhui University of Science and Technology, Huainan 232001, China*
[2] *School of Mechanical and Electrical Engineering, Huainan Normal University, Huainan 232001, China*

ABSTRACT: Addressing the challenge of suppressing common-mode (CM) and differential-mode (DM) electromagnetic interference (EMI) in interior permanent magnet synchronous motor (IPMSM) drive systems, as well as the shortcomings of traditional methods in dynamic response and harmonic suppression, this paper proposes a comprehensive suppression strategy that integrates an active common-mode filter (ACF) with a modified harmonic suppression reaching law (M-RL). By establishing the CM/DM equivalent circuits of the inverter-motor system, the mechanism through which high-frequency parasitic parameters affect interference propagation is elucidated. Based on this, an ACF structure with adaptive impedance matching capability is designed, effectively suppressing the peak common-mode voltage and broadening the filtering bandwidth. Furthermore, the M-RL algorithm, which incorporates a saturation function and harmonic weighting factors, is proposed. This algorithm significantly suppresses differential-mode voltage harmonics by dynamically adjusting the sliding mode convergence speed and harmonic gain. Simulated and experimental results demonstrate that, compared to traditional passive filters and fixed-gain sliding mode control, the proposed strategy reduces the peak common-mode voltage spectrum by 25.74 dBμV and the peak differential-mode voltage spectrum by 30.39 dBμV. The proposed M-RL itself reduces the current total harmonic distortion (THD) by 5579% and shortens the system dynamic response time to 0.01 seconds. This research provides effective theoretical and technical support for the electromagnetic compatibility (EMC) design of high-performance motor drive systems.

1. INTRODUCTION

With the rapid development of modern power electronics technology, the continuous increase in the switching frequency of power semiconductor devices has significantly improved the dynamic response and operational efficiency of electric motors. However, it has also introduced complex EMC challenges [1]. In high-frequency PWM-controlled environments, the rapid voltage transitions generated by the inverter not only induce common-mode voltage through the parasitic capacitance between the motor casing and ground, resulting in common-mode leakage currents with amplitudes of several amperes, but also cause a series of negative effects, such as shaft voltage and bearing current, which will lead to excessive bearing loss, conductive EMI, and even overvoltage at the motor terminal. Relevant studies have shown that the common-mode voltage generated by PWM inverters has high dv/dt, and the high-frequency leakage current caused by it will also reduce the service life of the motor bearing and the reliability of the entire drive system, as well as generate differential-mode interference voltage across the line impedances between phases. These high-frequency characteristics can easily affect the signal integrity of the control system through conductive coupling. As the frequency increases, high-frequency signals in dense wiring environments are prone to crosstalk, which is a type of conductive coupling. This kind of interference will cause signal distortion, reduce signal quality, and even affect the normal operation of the circuit if not controlled. In addition, conductive coupling can also lead to issues such as signal reflection and increased conduction loss, further damaging the signal integrity of the control system [2].

Permanent magnet synchronous motors (PMSMs) are often driven by voltage-source inverters. Nevertheless, the high dv/dt common-mode voltage and EMI issues caused by power switching devices severely affect system reliability. Approaches aimed at mitigating high-frequency interference predominantly employ passive RLC filters. Ref. [3] utilized a combination of passive components to establish a basic filtering path, demonstrating that the low-pass characteristics of capacitors can attenuate common-mode noise. However, this approach did not account for the influence of actual parasitic parameters, leading to a significant gap between high-frequency performance analysis and practical results. Ref. [4] further pointed out that passive filters are sensitive to parasitic parameters and are physically large; particularly, increasing capacitance values leads to parasitic inductance that causes resonance frequency shift, thereby limiting their applicability over a broad frequency range. Still, no effective method for suppressing or compensating parasitic parameters was proposed. In recent years, active EMI filters (AEFs) have garnered widespread attention due to their ability to

* Corresponding author: Wenyan Nie (wynie5240@163.com).

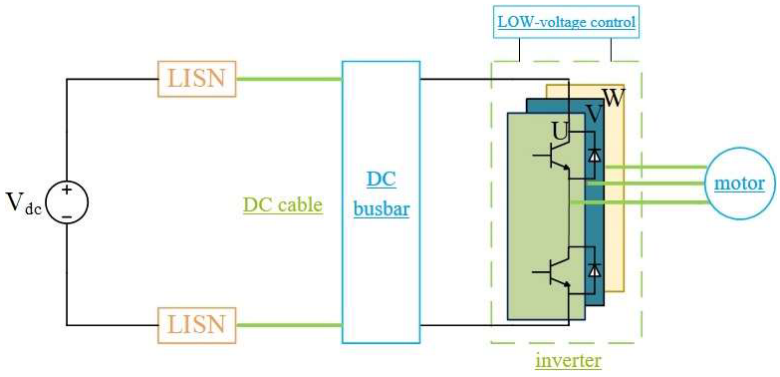

FIGURE 1. Block diagram of the motor drive system.

enhance high-frequency attenuation characteristics, reduce the size of passive components, and improve stability. Ref. [5] proposed a current-compensation-type AEF, showing that this structure can effectively suppress common-mode noise at the power supply end. However, it did not consider the propagation characteristics of high-frequency interference at the motor end, resulting in a limited suppression mode. Ref. [6] designed a voltage-compensation-type AEF, which is more suitable for suppressing interference at the motor terminal. Nonetheless, it failed to address the coordinated suppression of common-mode and differential-mode interference and exhibited limited effectiveness in suppressing noise at the power supply end. Moreover, such methods typically require integrating sensors directly into the DC bus. Ref. [7] noted that this approach is prone to magnetic core saturation and increases volume, but did not propose effective measures to reduce the system size without compromising performance. Additionally, some transformer-less AEF topologies have been employed to reduce system volume. Ref. [8] introduced a transformer-less AEF structure that achieves a compact form factor. However, it heavily relies on accurate extraction of the system's common-mode impedance, making it susceptible to performance degradation in practical applications due to parameter drift. Ref. [9] investigated the application of an ACF at the motor end, demonstrating effective suppression of interference in certain frequency bands. Still, it showed limited suppression of high-frequency noise at the power supply end and did not explore integration with control strategies to enhance system dynamic response. Ref. [10] further explored an active-passive hybrid filtering architecture, which balances high-frequency attenuation and volume constraints. However, it still fell short of unifying interference suppression with dynamic performance and lacked an in-depth mechanism for differential-mode interference suppression. Ref. [11] proposed an active filter design method based on impedance reshaping, improving filter stability. Yet, it did not consider the coupling effects with the motor control loop, making it difficult to apply directly in high-performance servo scenarios.

This paper takes an IPMSM drive system based on a voltage-source inverter as the research object and proposes an active compensation filter formed by integrating an active compensation circuit with a passive LC filter, combined with a modified harmonic suppression reaching law, to establish a software-hardware collaborative comprehensive electromagnetic interference suppression strategy. This strategy not only suppresses common-mode and differential-mode interference on both the motor side and the power supply side simultaneously, but also significantly improves high-frequency filtering performance over a wide frequency range compared with traditional passive LC filters. Moreover, through the low-frequency high-impedance characteristic of the active compensation circuit and the dynamic damping term in the M-RL, the phase margin of the system is enhanced. The strategy demonstrates comprehensive advantages in electromagnetic compatibility, high-frequency filtering capability, and dynamic stability.

2. ANALYSIS OF ELECTROMAGNETIC INTERFERENCE IN IPMSM DRIVE SYSTEMS

2.1. Composition of Motor Drive System

The system architecture, as illustrated in Fig. 1, consists of a high-voltage power drive loop and a low-voltage control circuit control system. The high-voltage loop originates from the traction battery, whose power travels sequentially through the LISN [12, 13], DC busbar, and inverter, where DC-AC conversion takes place to drive the motor. The low-voltage control system, supplied by a 12 V battery, regulates the high-voltage drive loop by transmitting commands generated by the vector controller [14].

2.2. Analysis of System Interference Sources and Propagation Paths

The EMI in the system originates primarily from the inverter and the motor. The rapid switching action of IGBTs in the inverter excites parasitic components, generating high-frequency electric and magnetic field interference. Meanwhile, the characteristics of the motor itself influence the coupling path and spectral composition of the interference [15]. These interferences are ultimately conducted through power and signal lines, manifesting as two fundamental modes: CM and DM.

Common-mode interference in motor drive systems is primarily generated by the interaction between instantaneous transient voltages during switching operations and the inherent parasitic capacitances within the system. These parasitic capacitances include those between the IGBT modules and the heat

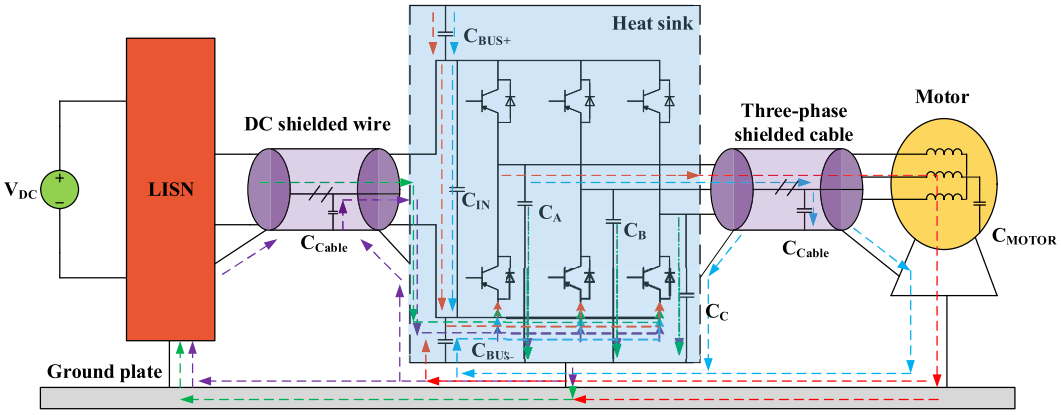

FIGURE 2. Common-mode conducted interference path.

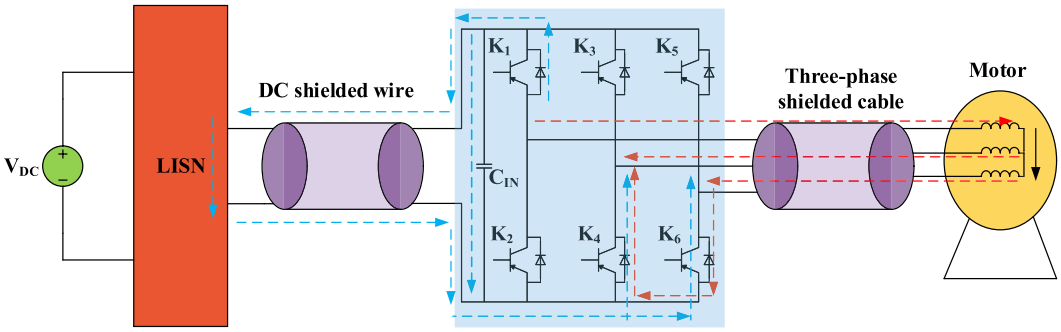

FIGURE 3. Differential-mode conducted interference path.

sink, between the DC busbar and the heat sink, between the motor windings and the chassis, as well as between the power cables and the shielding layer, among others. The common-mode conducted interference path within the system is illustrated in Fig. 2.

Differential-mode interference in motor drives is primarily formed by the interaction between the di/dt generated during the switching transitions, turn-on and turn-off of power semiconductor devices, and the stray inductance present within the system. When switches K1, K4, and K6 are turned on, the path of differential-mode conducted interference is illustrated in Fig. 3.

2.3. Multi-Domain Co-Simulation Modeling of EMI in IPMSM Drives

To overcome the limitations of traditional simulation methods in analyzing complex systems [16], this study adopts an integrated approach combining high-fidelity finite element simulation and mathematical modeling. IPMSM as the research object, a multi-domain co-simulation framework incorporating Maxwell for electromagnetic field analysis, Simplorer for power circuit simulation, and Simulink for control modeling, is established to effectively capture the cross-coupling effects among. In this framework, Maxwell is responsible for building the finite element simulation model of the motor, Simplorer serves as the bridge connecting Maxwell and Simulink to realize the construction of the power circuit, and Simulink provides control algorithms such as PID and pole placement adaptive control. electromagnetic, electrical, and control domains.

A comprehensive model for analyzing EMI in the motor drive system was developed using the ANSYS Simplorer platform. The model incorporates the motor finite element model from Maxwell and the control algorithm model from Simulink, creating a co-simulation framework. In this framework, inverter control commands are generated by Simulink, while motor electromagnetic properties are derived from Maxwell. It should be emphasized that the equivalent impedance of the motor windings, including resistance, high-frequency inductance, and parasitic capacitance to ground, varies significantly with frequency: at low frequencies, resistance dominates; as frequency increases, skin and proximity effects increase the AC resistance, inter-turn distributed capacitance creates low-impedance paths, and high-frequency inductance exhibits nonlinear behavior due to magnetic saturation and eddy-current losses. These frequency-dependent characteristics have been accurately extracted via frequency-domain finite-element analysis in Maxwell and directly imported into the Simplorer circuit model. Real-time data exchange is enabled through a dedicated data interface built into the co-simulation platform, whereby critical parameters computed by Simplorer are returned to Simulink for closed-loop control, resulting in a high-fidelity electromechanical simulation loop. The setup is depicted in Fig. 4.

Electromagnetic interference of the system was simulated via the aforementioned Simplorer motor drive system co-

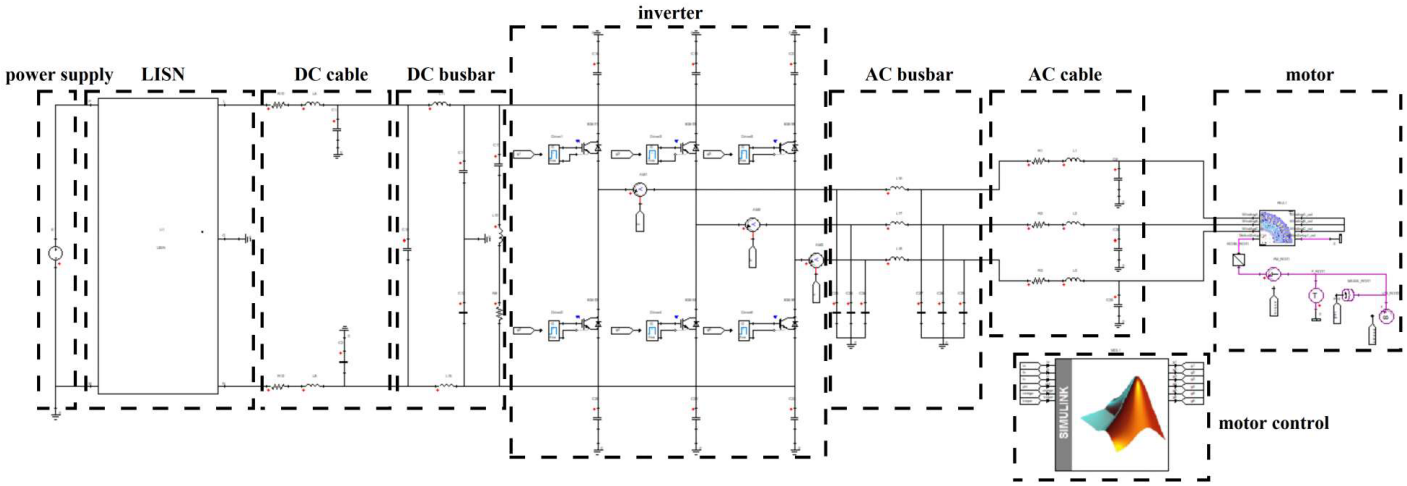

FIGURE 4. Simplorer co-simulation platform for the motor drive system.

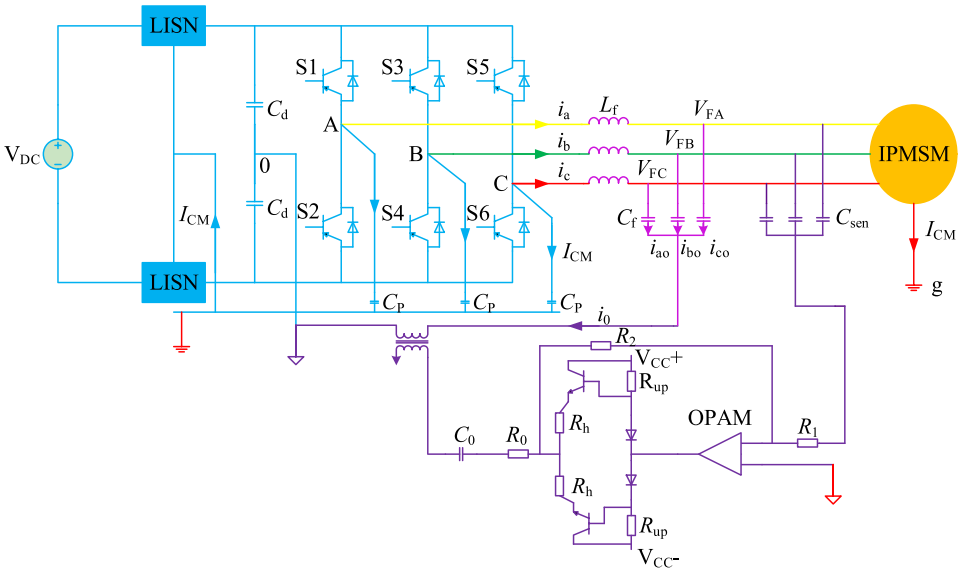

FIGURE 5. Schematic diagram of the IPMSM drive system based on the ACF.

simulation platform, with an IPMSM integrated with hairpin windings employed for the study. The simulation results for common-mode and differential-mode interference are presented in Fig. 6 and Fig. 8, respectively.

3. ACTIVE COMMON-MODE FILTER

The ACF proposed in this paper consists of a three-phase passive LC filter and an active compensation circuit connected in series. As a typical series-connected hybrid filtering structure, the passive LC filter, which is generally composed of capacitors, inductors, and resistors, and is commonly used for harmonic compensation and reactive power compensation, works together with the active compensation circuit. Its core function is to utilize the active circuit to present low impedance at high frequencies to suppress common-mode harmonics, which can significantly enhance the filtering effect of the passive LC filter. while maintaining high impedance at low frequencies to avoid adverse effects. The system schematic is shown in Fig. 5.

3.1. LC Filter

In Fig. 5, the three-phase output voltages of the LC filter with respect to the midpoint of the DC bus are given by:

$$\begin{cases} V_{FAO} = \frac{1}{C_f}\int i_{ao}\mathrm{d}t \\ V_{FBO} = \frac{1}{C_f}\int i_{bo}\mathrm{d}t \\ V_{FCO} = \frac{1}{C_f}\int i_{co}\mathrm{d}t \end{cases} \tag{1}$$

where V_{FAO}, V_{FBO}, and V_{FCO} denote the three-phase output voltages of the filter. The current i_o flowing between the midpoint of the filter capacitors and the midpoint of the DC-link support capacitors is expressed as:

$$i_{ao} + i_{bo} + i_{co} = i_o \tag{2}$$

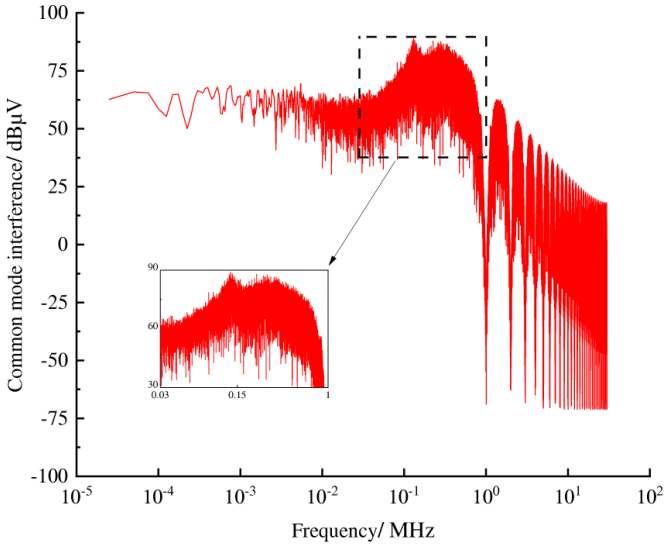

FIGURE 6. System common-mode interference spectrum.

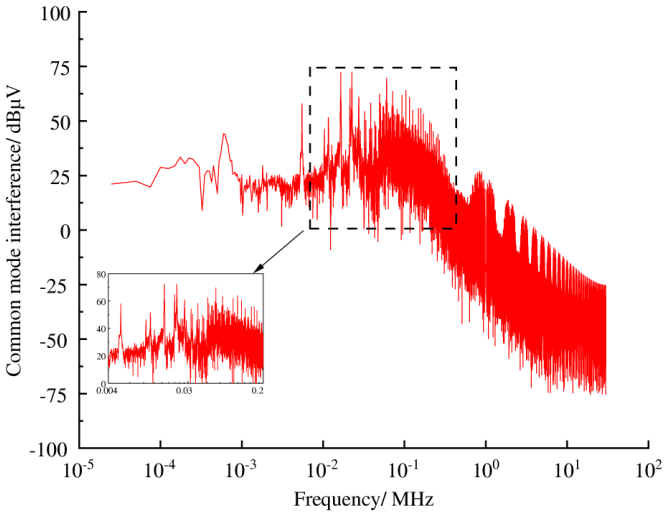

FIGURE 7. Common-mode interference spectrum of the system with ACF integrated.

Combining Equation (2) and neglecting the influence of cable impedance, the output voltage V_{MCM} of the filter capacitor branch can be expressed as the common-mode voltage at the motor terminal:

$$V_{\mathrm{MCM}} = \frac{1}{3}\left(V_{\mathrm{FAO}} + V_{\mathrm{FBO}} + V_{\mathrm{FCO}}\right) = \frac{1}{3C_f}\int i_0 \mathrm{d}t \quad (3)$$

It follows that the appropriate selection of the filter capacitance C_f can significantly reduce the common-mode voltage at the motor terminals.

3.2. Active Compensation Circuit

The active compensation circuit primarily consists of a sampling capacitor C_{sen}, a sampling resistor R_1, a feedback resistor R_2, an operational amplifier (OPAM), a push-pull amplifier circuit, a voltage converter, an output resistor R, and an output capacitor C. Its main functions include sampling, amplifying, and compensating the common-mode voltage in the drive system. It should be noted that non-ideal characteristics of practical operational amplifiers, e.g., temperature drift, input bias current noise, and voltage noise, may have a certain impact on the compensation accuracy at high frequencies.

The signal from the terminals undergoes inverting amplification through the OPAM, and the compensated signal is subsequently injected into the filter capacitor branch. The compensation voltage V_A can be expressed as:

$$V_{\mathrm{A}} = \frac{R_1}{Z_{\mathrm{sen}}} G V_{\mathrm{inc}} \quad (4)$$

where V_{inc} denotes the voltage across the filter capacitor; Z_{sen} represents the impedance of the sampling capacitor C_{sen}, and G represents the total gain of the active compensation circuit, expressed as:

$$G = -\frac{j\omega k N L_{\mathrm{inj}} A_{\mathrm{v}}}{\frac{1}{j\omega C_{\mathrm{o}}} + R_{\mathrm{o}} + j\omega L_{\mathrm{inj}}} \quad (5)$$

where k denotes the coupling coefficient of the voltage converter; N represents the turns ratio of the windings; L_{inj} indicates the magnetic core inductance of the voltage converter; and A_v signifies the closed-loop amplification gain of the OPAM, which can be expressed as:

$$A_v = \frac{-A_{\mathrm{op}} R_2}{A_{\mathrm{op}} Z_{\mathrm{sen}} + (R_2 + Z_{\mathrm{sen}})\left(1 + j\frac{\omega}{\omega_{\mathrm{p1}}}\right)\left(1 + j\frac{\omega}{\omega_{\mathrm{p2}}}\right)} \quad (6)$$

where A_{op} represents the open-loop amplification factor of the OPAM; ω_{p1} and ω_{p2} denote the two pole frequencies of the OPAM, with $\omega_{\mathrm{p1}} \gg \omega_{\mathrm{p1}}$.

3.3. Simulation Analysis

To evaluate the ACF performance, a complete drive system model incorporating the ACF was constructed in the ANSYS/Simplorer co-simulation platform. The switching frequency of the power devices in the voltage-source inverter is set to 10 kHz, and the space vector pulse width modulation strategy is adopted. The main system parameters are as follows: the DC bus input voltage is 300 V, the rated power is 5 kW, the electrical frequency is 50 Hz, the rated speed is 3000 r/min, and the control sampling frequency is 10 kHz. Regarding the parasitic parameters of the DC busbar, the equivalent series inductance is 50 nH and the equivalent series resistance is 5 mΩ. For the inverter part, the parasitic capacitance of the IGBT module is 100 pF; the parasitic capacitance between the IGBT module and the heat sink is 30 pF; and the parasitic capacitance between the DC busbar and the heat sink is 20 pF. The parasitic capacitance between the motor stator winding and the housing is 3.6 nF. For the power cables, the parasitic capacitance between each phase cable and the shielding layer is 100 pF/m, and the series inductance per phase is 0.5 μH/m. In the proposed ACF, the sampling capacitor is 10 nF, the sampling resistor R1 is 1 kΩ, the feedback resistor R2 is 10 kΩ, the output resistor R0 is 50 Ω,

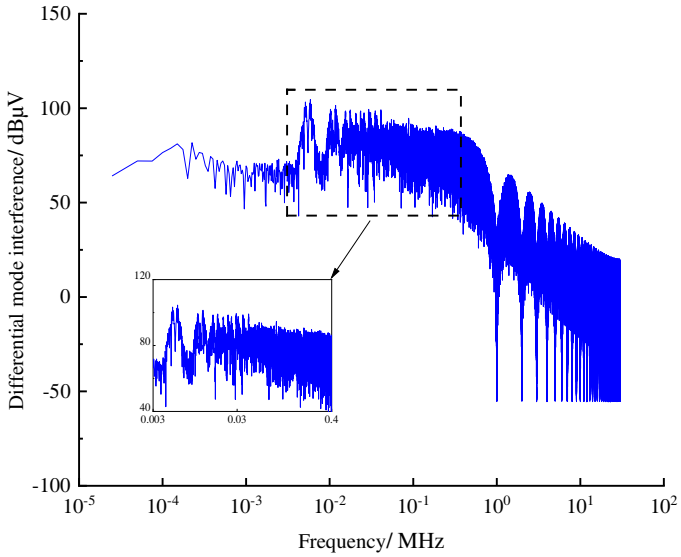

FIGURE 8. System differential-mode interference spectrum.

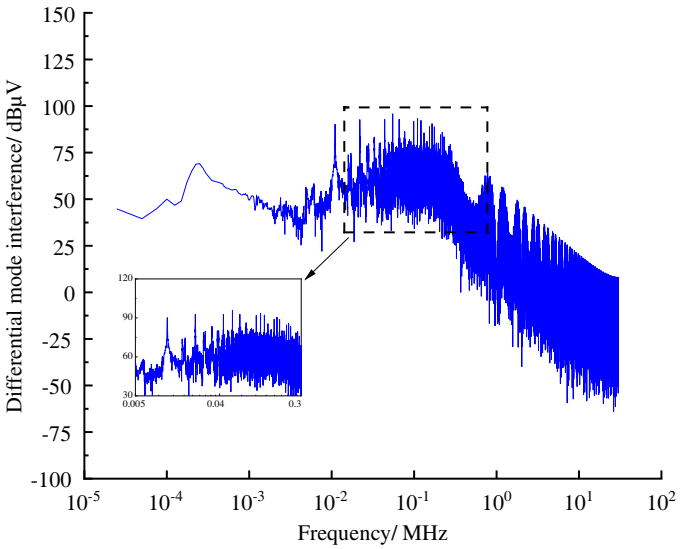

FIGURE 9. Common-mode interference spectrum of the system with ACF integrated.

the output capacitor C0 is 1 μF, the filter inductor Lf is 0.1 mH, and the filter capacitor Cf is 0.47 μF. By integrating the ACF into the common-mode path, its dynamic behavior and EMI suppression effectiveness were analyzed. The simulation focused on quantitatively assessing the improvement in the spectral distributions of both the common-mode voltage (CMV) and differential-mode voltage (DMV) at the DC bus. The results are shown in Fig. 7 and Fig. 9.

The comparison of Fig. 7 and Fig. 9 with Fig. 6 and Fig. 8 reveals that the introduction of the active common-mode filter significantly suppresses electromagnetic interference in the system. The ACF demonstrates notable advantages in mitigating common-mode interference across a wide frequency range. However, its effectiveness in attenuating differential-mode interference remains limited, indicating a need for supplementary measures to address DM noise.

It should be noted that even when the active compensation circuit is disabled (e.g., by setting the op-amp supply voltages to zero or setting the gain to zero), the proposed ACF structure still includes the passive LC filter formed by L_f and C_f as well as the sampling branch C_{sen} and R_1. These passive components alone provide a certain degree of highfrequency commonmode attenuation; however, due to parasitic parameters, the filtering performance of a standalone passive filter degrades significantly at high frequencies, which is exactly why active compensation is introduced. Furthermore, the fact that an active commonmode filter reduces differentialmode interference may seem counterintuitive. The underlying mechanism is that by sensing the commonmode voltage and injecting a compensating signal, the ACF indirectly improves the symmetry of the threephase inverter output voltage. Since differentialmode interference is closely related to the imbalance among the phase voltages, effective suppression of the commonmode voltage consequently reduces the harmonic content of the differentialmode voltage. This mechanism is validated by the comparison between the merged figures, Figs. 7/9 vs. Figs. 6/8, and is also supported by existing literature, which reports a similar sidebenefit of commonmode filtering on differentialmode emissions. Therefore, only the complete ACF achieves cooperative wideband suppression of both commonmode and differentialmode interference.

4. HARMONIC SUPPRESSION REACHING LAW

However, the active common-mode filter exhibits limited suppression capability against differential-mode interference. Under high-frequency PWM operation, differential-mode interference can couple into the control system, degrading its dynamic performance and stability. Furthermore, existing control strategies often respond sluggishly to such high-frequency disturbances and lack sufficient robustness, making it difficult to achieve coordinated suppression of both differential-mode interference (DMI) and common-mode interference (CMI).

In order to address the above limitation, a modified harmonic suppression reaching law (M-RL) is proposed for the controller. The system's closed-loop vector diagram is shown in Figure 10. This reaching law introduces three innovations over the conventional sliding-mode reaching law: replacing the sign function with a hyperbolic tangent saturation function to achieve smooth switching and eliminate chattering; introducing a dynamic damping term for adaptive gain adjustment; and adding a harmonic feedforward integral term to actively compensate high-frequency differential-mode disturbances. By incorporating dynamic damping, harmonic feedforward, and smooth switching, the M-RL enhances the system's high-frequency disturbance rejection capability and mitigates SMC chattering. The synergy between the M-RL (software) and the ACF (hardware) collectively extends the EMI suppression bandwidth and boosts the system's electromagnetic compatibility and robustness.

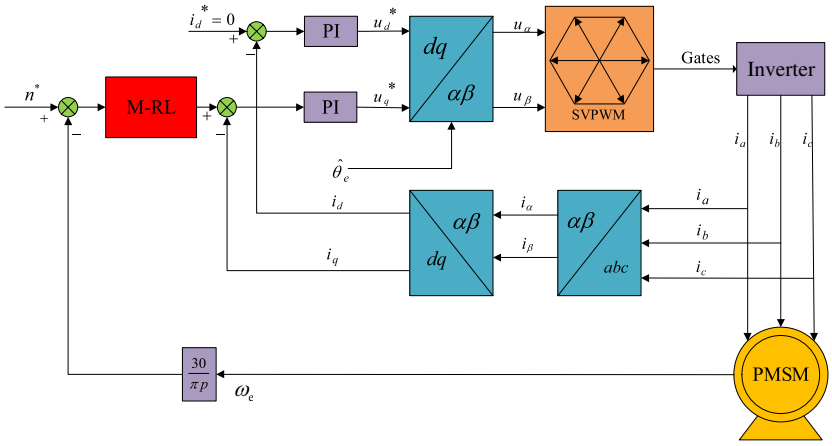

FIGURE 10. Closed-loop vector diagram of the M-RL-based control system.

4.1. Structural Analysis

The expression for the M-RL is given as follows:

$$\dot{s} = -k\tanh\left(\frac{s}{\varepsilon}\right) - q(t)s + \eta\int_0^t \Delta i_h(\tau)d\tau \qquad (7)$$

where s denotes the sliding surface function; k represents the sliding mode gain, satisfying $k > 0$; ε is the boundary layer parameter, with $\varepsilon > 0$; $q(t)$ denotes the dynamic damping function; Δi_h represents the high-frequency current variation; and η signifies the harmonic compensation coefficient.

Traditional reaching laws often adopt the form $\dot{s} = -k\text{sign}(s)$. While this structure offers fast convergence, its aggressive control switching tends to excite high-frequency oscillations in the system. In contrast, the smooth switching term $-k\tanh\left(\frac{s}{\varepsilon}\right)$ employed in this work provides significant advantages: when $|s| \gg \varepsilon$, the convergence speed remains comparable to that of conventional sliding mode control, whereas within the region $|s| \ll \varepsilon$, the function behaves approximately linearly, effectively mitigating chattering and enhancing system smoothness. Additionally, the continuous differentiability of this term facilitates Lyapunov-based stability analysis, simplifying formal proof of system stability. The term $-q(t)s$ introduces dynamic adaptive characteristics, where $q(t)$ can be adjusted in real time based on the disturbance intensity or error evolution. The term $\eta\int_0^t \Delta i_h(\tau)d\tau$ represents a disturbance compensation mechanism designed to capture the trend of high-frequency current disturbances at the motor terminal. Here, $\Delta i_h(\mathrm{t}) = i_h(\mathrm{t}-\delta) - i_{h-1}(\mathrm{t}-\delta)$ defines the high-frequency disturbance component, with δ being the observation time interval. The integration process helps suppress high-frequency peaks, and the inclusion of this term on the right-hand side of the control law effectively performs "counter-injection" to counteract the source of disturbance.

4.2. Analysis of Electromagnetic Interference Suppression Mechanism

Differential-mode interference is caused by imbalances in the flow of drive current along the positive and negative lines, nonlinear loads, and switching devices, and primarily propagates between the two-phase conductors [17]. Its frequency distribution is mainly concentrated around the pulse width modulation (PWM) frequency and its harmonics, with common peak values reaching several tens of dBμV. The M-RL avoids exciting high-frequency DMI through its smooth switching term, preventing high-frequency resonance or amplification effects and helping to stabilize the drive output. The dynamic damping term automatically adjusts the control gain based on the rate of change of the differential-mode disturbance, enhancing the local robustness of the response to DMI. The feedforward compensation term actively identifies fast disturbance components in the DMI and provides feedforward suppression compensation to the system, weakening the source of interference energy. Common-mode interference leaks through the grounding system at higher frequencies. The M-RL primarily suppresses voltage spikes caused by sudden frequency changes through its integral prediction term. When combined with the ACF structure, the M-RL forms an inner control loop to suppress interference sources, while the ACF constitutes an outer hardware loop to dissipate interference energy. Together, they form an inner-outer loop coordination mechanism that effectively expands the operating bandwidth for EMI suppression.

4.3. Experimental Analysis

A comparative analysis of the systems is performed across three dimensions: dynamic response, current harmonic characteristics, and electromagnetic interference suppression. Comparative tests are conducted on the M-RL and traditional Sliding Mode Control (SMC) strategies via the Matlab/Simulink platform. The speed dynamic performance of both control strategies under sudden load disturbance conditions is depicted in Fig. 11.

Conventional SMC exhibits significant inertial overshoot due to the discontinuous switching of its reaching law, resulting in a speed overshoot of 32.1%. In contrast, the M-RL reduces the overshoot to 6.6% by replacing the sign function with a hyperbolic tangent saturation function. The speed regulation time of traditional SMC is 0.05 s, accompanied by oscillatory decay. Owing to the feedforward compensation achieved through a disturbance differential observer, the M-RL shortens the reg-

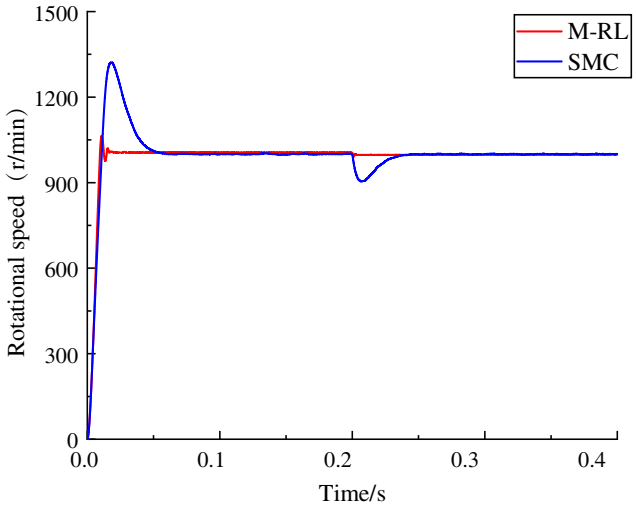

FIGURE 11. Speed response diagram.

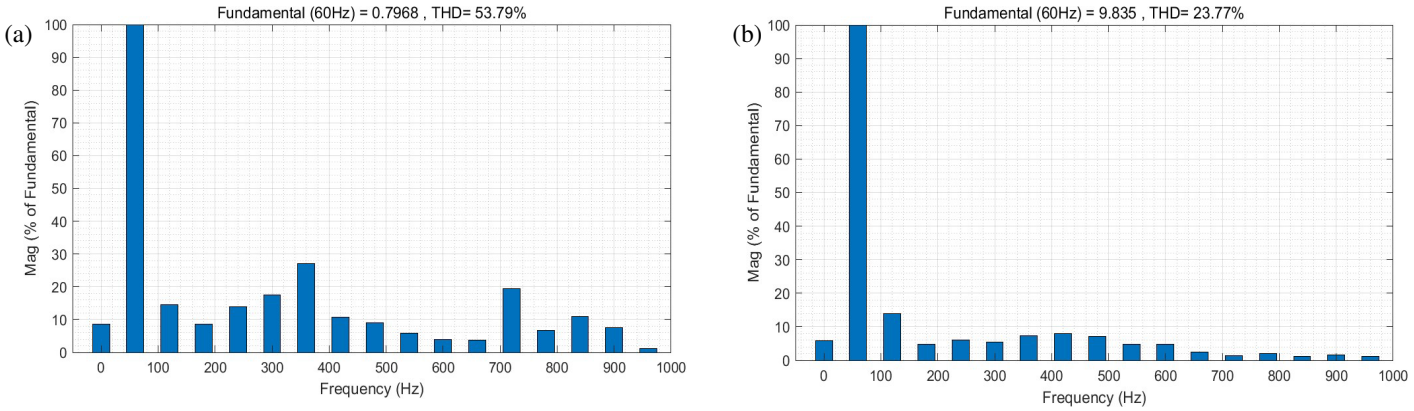

FIGURE 12. Comparison of total harmonic distortion. (a) THD of conventional SMC. (b) THD of M-RL.

ulation time to 0.01 s and improves the smoothness of the dynamic response by 80%.

Fast Fourier transform (FFT) analysis was performed on the three-phase currents during steady-state operation under both control strategies (sampling frequency: 60 Hz). The THD results are shown in Fig. 12. As observed in Figs. 12(a) and 12(b), the traditional SMC method yields a THD of 53.79%, with prominent harmonic clusters. In contrast, the M-RL method reduces the THD to 23.77% by smoothing the q-axis current reference through an adaptive boundary layer technology, thereby effectively suppressing harmonics.

A multi-physics co-simulation was conducted by integrating the M-RL-based motor control module developed in Matlab/Simulink with the circuit model in Ansys/Simplorer and the finite element motor model in Ansys/Maxwell. The electromagnetic interference of the IPMSM drive system was evaluated, and the spectral distributions of the common-mode voltage and differential-mode voltage at the critical DC busbar are shown in Fig. 13 and Fig. 14, respectively.

Analysis of Fig. 14 indicates that, compared to the ACF common-mode filter alone, the introduction of the M-RL control strategy significantly enhances the suppression of both common-mode and differential-mode interference in the system. Notably, it addresses the limitations of the ACF in mitigating differential-mode interference. Furthermore, compared to the pre-optimized drive system, the optimized system demonstrates markedly suppressed electromagnetic interference, fully complying with the limits specified in international standards for electromagnetic emissions from electric vehicles and their high- and low-voltage components. A comparison of interference data for the three systems is presented in Table 1.

In a traditional built-in permanent magnet synchronous motor drive system, the common-mode interference voltage spectrum and differential-mode interference voltage spectrum are 88.85 dBμV and 104.52 dBμV, respectively, indicating a high level of EMI. To suppress common-mode interference, after introducing an ACF into the system, the common-mode and differential-mode interference voltage spectra are reduced to 72.38 dBμV and 95.69 dBμV, respectively, with a significant suppression effect on common-mode interference, a reduction of 18.5%. To further improve the differential-mode interference suppression capability, the system adopted an improved M-RL control strategy. After applying the M-RL strategy, the common-mode and differential-mode interference voltage spectra are further reduced to 63.11 dBμV and 74.13 dBμV, respectively. Comparative data analysis shows that in terms of common-mode interference suppression, com-

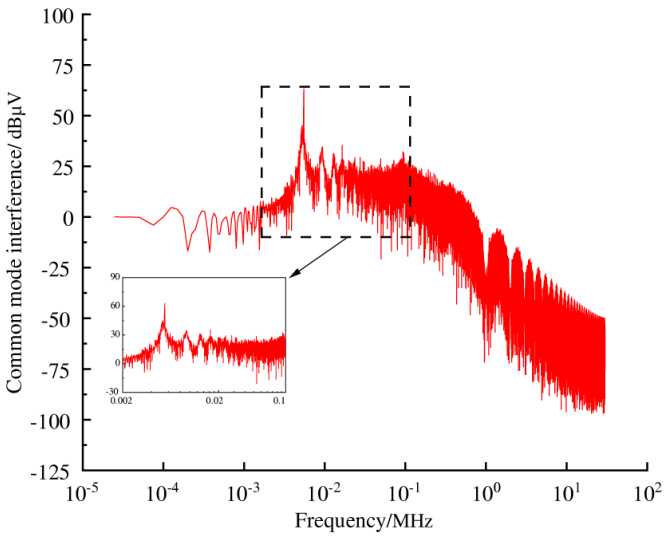

FIGURE 13. Common-mode interference spectrum of the system with M-RL incorporated.

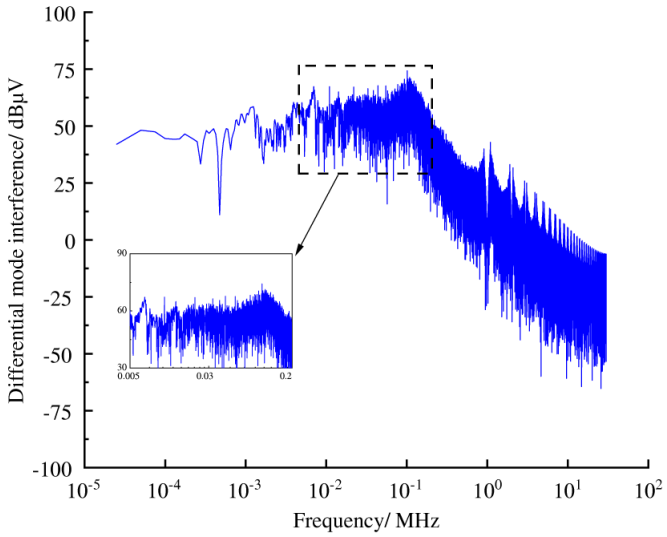

FIGURE 14. Differential-mode interference spectrum of the system with M-RL incorporated.

TABLE 1. Simulated electromagnetic interference data of motor drive systems.

System name	Common-mode interference/dBμV	Differential-mode interference/dBμV	CISPR 25 Class 1 limits(dBμV)	Whether it meet international standards
Conventional drive system	88.85	104.52	86 (0.5–30 MHz)	Does not meet
ACF-based drive system	72.38	95.69	86	Differential mode does not meet
ACF and M-RL based drive system	63.11	74.13	86	meeet

pared with the traditional drive system, the M-RL strategy reduces the common-mode interference voltage by 28.9%; compared with the system using only ACF, it further reduces it by 10.4%. In terms of differential-mode interference suppression, compared with the traditional drive system, the M-RL strategy reduces the differential-mode interference voltage by 29.1%; compared with the system using only ACF, it further reduces it by 20.7%

5. CONCLUSION

This study addresses the severe electromagnetic interference issues in IPMSM drive systems. Simulations measured the common-mode and differential-mode interference voltage spectra of a conventional system. Through the innovative introduction of an ACF, common-mode interference was significantly reduced, and differential-mode interference was simultaneously suppressed. To further break through the limitations in differential-mode interference suppression, an M-RL control strategy was proposed, establishing a collaborative mechanism of "active filtering + intelligent control." Experimental validation demonstrated that, on a multi-domain co-simulation platform integrating Maxwell finite element analysis, Simplorer circuit simulation, and Simulink control modeling, the collaborative scheme achieved deep suppression of both common-mode and differential-mode interference. This approach reveals the common-mode and differential-mode coupling mechanism at the interference source level and realizes EMI suppression through dual pathways: switching sequence optimization and current compensation. The research provides an EMC solution with both theoretical innovation and engineering practicality for high-power-density motor drive systems, particularly suitable for stringent electromagnetic environments, such as electric vehicle powertrains. Future work may extend to multi-objective collaborative optimization leveraging the characteristics of wide-bandgap power devices.

ACKNOWLEDGEMENT

This work was supported in part by the Natural Science Research Project of Anhui Educational Committee under Grant no. 2025AHGXZK31006, in part by the Research Foundation of Jiangsu Engineering Research Center for Bionics Control Technology and Equipment under No. FSKZ202503, in part by the Anhui International Joint Research Center for Ancient Architecture Intellisencing and Multi-Dimensional Modeling under No. GJZZX2025KF03.

REFERENCES

[1] Ramya, K., J. Gopalakrishnan, B. Chokkalingam, R. Verma, and L. Mihet-Popa, "A comprehensive evaluation and assessment practices of electromagnetic interferences in electric vehicle," *IEEE Access*, Vol. 13, 40 520–40 560, 2025.

[2] Muetze, A. and A. Binder, "Calculation of circulating bearing currents in machines of inverter-based drive systems," *IEEE Transactions on Industrial Electronics*, Vol. 54, No. 2, 932–938, 2007.

[3] Dai, L., W. Chen, X. Yang, M. Zheng, Y. Yang, and R. Wang, "A multi-function common mode choke based on active CM EMI filters for AC/DC power converters," *IEEE Access*, Vol. 7, 43 534–43 546, 2019.

[4] Zhang, Z. and A. M. Bazzi, "A virtual impedance enhancement based transformer-less active EMI filter for conducted EMI suppression in power converters," *IEEE Transactions on Power Electronics*, Vol. 37, No. 10, 11 962–11 973, 2022.

[5] Zhang, Y. and D. Jiang, "An active EMI filter in grounding circuit for DC side CM EMI suppression in motor drive system," *IEEE Transactions on Power Electronics*, Vol. 37, No. 3, 2983–2992, 2022.

[6] Wang, H., W. Chen, W. Chen, R. Cheng, Y. Huo, W. Du, and X. Yang, "A novel active EMI filter based on transfer common-mode noise to differential-mode noise," *IEEE Transactions on Power Electronics*, Vol. 40, No. 7, 8950–8955, 2025.

[7] Liu, J., Y. Zhang, D. Jiang, X. Zhao, and Z. Liu, "Insertion loss analysis and optimization of a current based common-mode active EMI filter," *IEEE Transactions on Power Electronics*, Vol. 39, No. 11, 14 353–14 362, 2024.

[8] Zhang, Z., Y. Hu, X. Chen, G. W. Jewell, and H. Li, "A review on conductive common-mode EMI suppression methods in inverter fed motor drives," *IEEE Access*, Vol. 9, 18 345–18 360, 2021.

[9] Takahashi, S., S. Ogasawara, M. Takemoto, K. Orikawa, and M. Tamate, "Common-mode voltage attenuation of an active common-mode filter in a motor drive system fed by a PWM inverter," *IEEE Transactions on Industry Applications*, Vol. 55, No. 3, 2721–2730, 2019.

[10] Han, Y., Z. Wu, and D. Wu, "Hybrid common-mode EMI filter design for electric vehicle traction inverters," *Chinese Journal of Electrical Engineering*, Vol. 8, No. 4, 52–60, 2022.

[11] Zhang, Y., Q. Li, and D. Jiang, "A motor CM impedance based transformerless active EMI filter for DC-side common-mode EMI suppression in motor drive system," *IEEE Transactions on Power Electronics*, Vol. 35, No. 10, 10 238–10 248, 2020.

[12] Wan, L., A. D. Khilnani, X. Wu, X. Liu, S. A. Pignari, D. W. P. Thomas, M. Sumner, and F. Grassi, "Design of an LISN for low-frequency conducted emissions measurement," *IEEE Transactions on Electromagnetic Compatibility*, Vol. 67, No. 2, 351–361, 2025.

[13] BSI Standards Limited, "Vehicles, boats and internal combustion engines — Radio disturbance characteristics — Limits and methods of measurement for the protection of on-board receivers: CISPR 25:2021," *London: BSI Standards Limited*, 1–183, 2022.

[14] Sakunthala, S., R. Kiranmayi, and P. N. Mandadi, "A review on speed control of permanent magnet synchronous motor drive using different control techniques," in *2018 International Conference on Power, Energy, Control and Transmission Systems (ICPECTS)*, 97–102, Chennai, India, 2018.

[15] Zhai, L., S. Yang, G. Hu, and S. Wang, "Modeling on conducted electromagnetic interference for motor drive system of electric vehicle," *Transactions of Beijing Institute of Technology*, Vol. 42, No. 8, 824–833, 2022.

[16] Dobkin, D., E. Katz, D. Popovtzer, and I. Levi, "Emerging technologies," *ACM Journal on Emerging Technologies In Computing Systems*, Vol. 22, No. 1, 2026.

[17] Kumar, M. and K. Jayaraman, "Design of a modified single-stage and multistage EMI filter to attenuate common-mode and differential-mode noises in SiC inverter," *IEEE Journal of Emerging and Selected Topics in Power Electronics*, Vol. 10, No. 4, 4290–4302, 2022.